Proceedings of the Institution of Mechanical Engineers, Part J: Journal of Engineering Tribology

Transient elastohydrodynamic point contact analysis using a new coupled differential deflection method Part 2: Results

M. J. A. Holmes, H. P. Evans, T. G. Hughes and R. W. Snidle

The online version of this article can be found at:

Published by:

\$SAGE

On behalf of:

Institution of MECHANICAL ENGINEERS

Institution of Mechanical Engineers

Additional services and information for *Proceedings of the Institution of Mechanical Engineers, Part J: Journal of Engineering Tribology* can be found at:

Email Alerts: http://pij.sagepub.com/cgi/alerts

Subscriptions: http://pij.sagepub.com/subscriptions

Reprints: http://www.sagepub.com/journalsReprints.nav

Permissions: http://www.sagepub.com/journalsPermissions.nav

Citations: http://pij.sagepub.com/content/217/4/305.refs.html

>> Version of Record - Apr 1, 2003

What is This?

Transient elastohydrodynamic point contact analysis using a new coupled differential deflection method Part 2: results

M J A Holmes, H P Evans[*]**, T G Hughes** and **R W Snidle**
Mechanical Engineering and Energy Studies Division, Cardiff School of Engineering, Cardiff University, Cardiff, Wales, UK

Abstract: The paper presents results obtained using a transient analysis technique for point contact elastohydrodynamic lubrication (EHL) problems based on a formulation that effectively couples the elastic and hydrodynamic equations. Results are presented for transverse ground surfaces in an elliptical contact that show severe film thinning at the transverse limits of the contact area. This thinning is caused by transverse (side) leakage of the lubricant from the contact in the remaining deep valley features. Comparison is made between the elliptical contact results on the entrainment centre-line and the equivalent line contact analysis. This confirms the importance of edge effects as a likely cause of film collapse and scuffing failure.

The surface profiles used in the analysis are taken from test discs used in scuffing experiments and from gears used in micropitting tests. Side leakage is found to be sufficiently severe to cause microasperity contact in the numerical examples presented. This contact mainly occurs close to the edges of the corresponding Hertzian area and correlates in position with the location at which scuffing is found to first occur in the earlier experiments.

Comparisons are made with other numerical results for point contact configurations with sinusoidally varying surface features obtained by Zhu (2000) and considerable differences are seen in the calculated extent of asperity contact. The differences are thought to be due to the simplified treatment of the lubrication equation adopted by Zhu.

Keywords: point contact EHL, non-Newtonian, transient, coupled method, differential deflection, side leakage

NOTATION

a, b	Hertzian contact dimensions (m)
E'	effective modulus of elasticity (Pa)
$f_{i,j}$	pressure influence coefficient in the differential deflection equation (m^{-1})
h	film thickness (m)
H_c	dimensionless film thickness $= h/R_x$, defined in reference [5]
n_c	number of neighbouring mesh points in discretization
p	pressure (Pa)
p_{hz}	maximum pressure in Hertzian contact (Pa)
R_x, R_y	radii of relative curvature in axis directions (m)
t	time (s)
u_{max}	surface velocity of the fastest moving surface in the x direction (m/s)
$\bar{U}, \bar{V}$	mean surface velocities in axis directions (m/s)
w	load for elliptical contact (N)
w'	load per unit length for the line contact (N/m)
W^*	dimensionless load $= w/(E'R_x^2)$, defined in reference [5]
x, y	coordinates in the contact plane (m)
α	viscosity/pressure coefficient (Pa^{-1})

Δt	timestep (s)
$\Delta x, \Delta y$	mesh spacing in coordinate directions (m)
η_0	viscosity at ambient pressure (Pa s)
λ	ratio of film thickness to composite surface roughness
ξ	slide–roll ratio
ρ	density (kg/m^3)
σ_x, σ_y	flow coefficients in axis directions (m s)
τ_0	non-Newtonian shear stress parameter (Pa)

1   INTRODUCTION

This paper presents theoretical results from the analysis of transient rough surface point contact problems obtained using the new coupled numerical formulation to the elastohydrodynamic lubrication (EHL) point contact problem described and validated in the companion paper [1]. The primary purpose of the paper is to demonstrate the strong side leakage effects that can take place in transverse finished elliptical contacts. In the case of smooth surfaces the EHL contact adopts a self-sealing configuration by developing side constrictions in the form of the familiar horseshoe shape measured in optical interferometry experiments. When significant transverse roughness features are present, however, this mechanism is unable to seal the transverse flow in the valley features of the roughness because the closest that the surfaces can be brought together is determined by physical contact of the asperity tip features. This mechanism of acute side leakage in rough contacts was proposed as the basis of an EHL failure model by the authors in a previous paper [2], following the observation that scuffing failure in such contacts invariably occurred at their edges [3]. This transverse boundary location is not subject to extreme temperature or pressure behaviour and its identification as the location of initial scuffing failure is a significant observation that identifies fluid film collapse as the originator of the thermal runaway that characterizes the scuffing mechanism.

In engineering practice the edge areas in gear contacts are subject to leakage of the form described above, but the load-bearing area is often treated as a line contact. Comparison of line and point contact results using surface profiles taken from experiments confirm that side leakage has very little influence except at the transverse limits of a contact. In practical gear contacts such failure may not be limited to the nominal edges of the contacts, but may occur away from the edges of teeth due to surface waviness features.

Finally, some detailed comparisons are made with published EHL point contact results that exhibit micro- and macrocontact. The cases considered are of surfaces with sinusoidal surface finish [4] and extreme load behaviour of smooth surfaces [5]. Significant differences are seen between the current work and the results published in references [4] and [5].

2   CONTACT ANALYSIS

The companion paper [1] discusses the way in which the hydrodynamic Reynolds equation

$$\frac{\partial}{\partial x}\left(\sigma_x \frac{\partial p}{\partial x}\right) + \frac{\partial}{\partial y}\left(\sigma_y \frac{\partial p}{\partial y}\right) - \frac{\partial(\rho \bar{U} h)}{\partial x} - \frac{\partial(\rho \bar{V} h)}{\partial y}$$
$$- \frac{\partial(\rho h)}{\partial t} = 0 \qquad (1)$$

and the deflection equation

$$\frac{\partial^2 h(x_i, y_j)}{\partial x^2} + \frac{\partial^2 h(x_i, y_j)}{\partial y^2}$$
$$= \frac{1}{R_x} + \frac{1}{R_y} + \frac{2}{\pi E'} \sum_{\text{all } k, l} f_{k-i, l-j} p_{k,l} \qquad (2)$$

are combined to form a coupled matrix problem where the pressure and film thickness at each point are primary variables to be solved for simultaneously. In the current point contact configuration these equations are solved by a novel coupled iterative scheme as described in reference [1]. A new feature of the results presented in the current paper is that of fluid film breakdown resulting in contact between the microasperities. Where contact occurs between the two surfaces the hydrodynamic film thickness is theoretically zero, although in practice there will typically be a boundary film that controls the local friction coefficient. Equation (1) arises from fundamental consideration of mass flow continuity of the fluid film, and at locations where the film thickness is zero there can be no such mass flow. The physical principle on which equation (1) is founded is thus not applicable at microcontact locations. Equation (2), however, is always applicable as it relates the pressure acting on the surfaces to their deflection irrespective of whether the pressure arises from a hydrodynamic film or from direct contact.

When equations (1) and (2) are discretized using finite element or finite difference methods they become algebraic equations relating the pressure and film thicknesses at neighbouring points. For the (i, j) node these are of the form

$$\sum_{k=0}^{n_c} A_k p_k + \sum_{k=0}^{n_c} B_k h_k = R_{i,j} \qquad (3)$$

$$\sum_{k=0}^{n_c} C_k p_k + \sum_{k=0}^{n_c} D_k h_k = E_{i,j} \qquad (4)$$

as discussed in reference [1]. In equations (3) and (4) the

suffix k represents the nodes contributing to the assembled equation at node (i, j) and $k = 0$ denotes that node. A_k and B_k are the pressure and film variable coefficients for the Reynolds equation (1) and n_c is the number of neighbouring nodes involved in the formulation. Similarly, C_k and D_k are the pressure and film variable coefficients for the differential deflection equation (2). In a finite difference discretization, equations (3) and (4) correspond to applying the finite difference equations at that mesh point. In a finite element hydrodynamic formulation, equation (3) results from the element fluid matrix assembly procedure.

To correctly include contact situations in the coupled methods described in references [1] and [6] the hydrodynamic equation (1) corresponding to the contacting point is removed from the solution scheme and replaced by the condition $h = 0$. This condition is effectively a prescribed displacement at the contacting point as far as the deflection equation is concerned so that the pressures obtained using that equation are consistent with the local film shape incorporating the prescribed deflection at the contacting point(s). Since the hydrodynamic equation has been removed from the scheme at the contacting point, the pressure developed there is a pressure boundary condition for the full-film areas on either side of the localized contact. The value of $h = 0$ is the required boundary value for the film thickness in the adjoining full-film areas.

For the line contact analysis [6] the problem matrix is solved with a standard elimination solver. To implement the procedure described above for this solution method it is necessary to re-order the hydrodynamic and elastic equations corresponding to the contacting point. Thus the elastic equation (2) relating h and p is written into the corresponding hydrodynamic row, and the original elastic equation row in the matrix becomes the condition $h = 0$. For the point contact analysis described in reference [1] this procedure is unnecessary as a suitable adjustment can be made within the iterative scheme. If a negative value for h is calculated in solving equations (3) and (4) at a mesh point during the iterative process, then it is set to zero and equation (4) is solved for the resulting pressure value.

This approach can be used to solve the dry contact problem using equation (2), as can be seen from the results for the smooth contact start-up analysis presented in reference [7]. This problem involves the simultaneous solution of full-film and dry contact areas because liquid is first entrained into a dry contact by motion of the surfaces. The iterative approach described above deals effectively with this situation, maintaining a dry contact pressure that remains essentially Hertzian away from the area where the contact shape is distorted by the entrained fluid. The comparison made in reference [7] with the elegant experimental work of Glovnea and Spikes [8] for this situation provides confirmation of the validity of the approach adopted.

3 RESULTS

3.1 Comparison of point and line contact solutions

Results were obtained using the method described above and in reference [1] for the rolling/sliding contact between two rough surfaces. The configuration examined was that of a contact corresponding to crowned discs used in experimental scuffing tests by Patching *et al.* [3] and others. The crowned finish is obtained using a generating process where the disc is brought into contact with the internal conical surface of a grinding wheel while rotated about its shaft axis, as described in reference [3]. This results in grinding finishing marks that are essentially in the transverse direction (i.e. perpendicular to the circumference of the disc). The grit paths are in reality circular, but with a radius that exceeds the disc thickness by a factor of about 10. Two such discs are loaded together in the scuffing experiments and the crown and disc radii are such that the radii of relative curvature are $R_x = 19.05$ mm and $R_y = 152.5$ mm, giving a contact aspect ratio of 3.91.

The line contact configuration adopted for comparison purposes was as examined by Tao *et al.* [9] and is specified in Table 1 along with all other operating condition parameters. The comparison was made on the basis that the geometrical features in the entrainment direction were equal, i.e. R_x and a, and the 5 per cent difference in the Hertzian pressure is an unavoidable difference due to the different contact configurations. A 4 per cent difference in η_0 between the cases was used to ensure equal smooth surface central film thickness values. This difference in η_0 was adopted for all the line and point contact comparisons reported in the paper. The rough surface data used are a series of equally spaced surface heights taken with a profilometer from experimental discs. The profiles used for the analyses presented are illustrated in Fig. 1, where in each case solid metal is below the profile. Trace A is a profile taken from a well run-in transverse ground disc used in scuffing experiments by Patching *et al.* [3].

Table 1 Operating conditions for the point and line contact comparisons

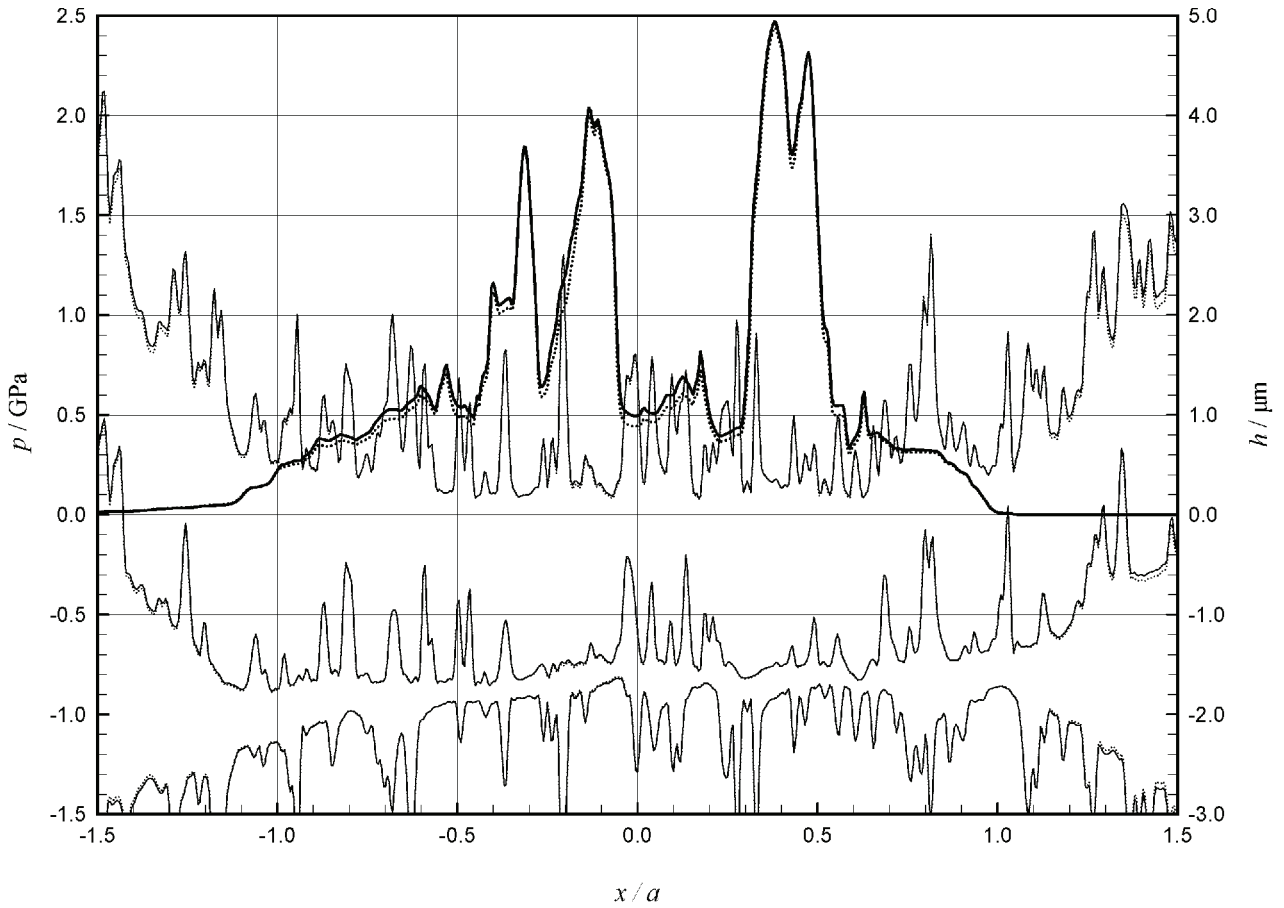|	Point contact	Line contact
R_x (mm)	19.05	19.05
R_y (mm)	150.5	∞
w, w'	962 N	526.6 kN/m
a (mm)	0.335	0.335
b (mm)	1.31	∞
p_{hz} (GPa)	1.05	1.0
E' (GPa)	227.3	
α (GPa^{-1})	11.1	
η_0 (Pa s)	0.005	0.0048
U (m/s)	25	
ξ	0.1, 0.25, 0.5	
τ_0 (MPa)	10	
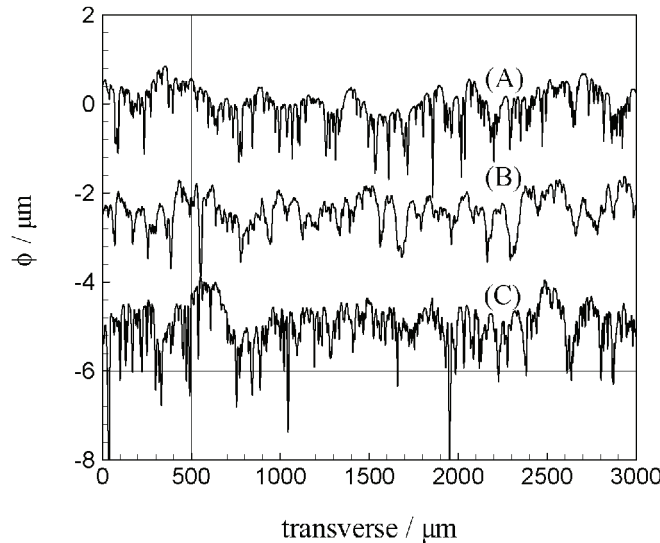
Fig. 1 Comparison of the surface roughness profiles used for the point and line contact analyses. The solid surface is below the profile

Traces B and C are taken from gear micropitting tests and have been run for several load stages, and as a result have become run-in to some extent, but close examination shows that they clearly have larger asperities than profile A. Traces A, B and C have R_a values of 0.32, 0.22 and 0.31 μm respectively. The lubricant modelled is Mobil Jet 2, a synthetic gas turbine lubricant used in earlier scuffing experiments [3], and the lubricant parameters used are as specified in Table 1. Intermediate heights that are required as the surfaces move through the contact are obtained using cubic spline interpolation, which ensures slope continuity at the measured points. Ensuring that the contact dimension, a, is identical for the point and line contact cases enables mesh sizes in the x direction to be specified that are exactly equal. This ensures that in the comparisons both rough surfaces are defined by exactly the same undeformed surface height at each mesh point in each of the two models.

The transient analysis is started from the smooth steady state solution and the rough surface features, which make the problem time dependent, are fed in with the moving surfaces from the inlet boundary position. Because of the different speeds of the two surfaces the time taken for both surfaces in the contact to become fully rough is that for the slowest of the two surfaces to move from the inlet boundary to the exit boundary. Figure 2 shows the pressure and film thickness obtained using the point and line contact models at a particular timestep when both surfaces are rough, with the roughness profile taken from profile A in Fig. 1. These variables are shown in the upper part of the figure and the two rough surfaces are seen below in their configuration at the current timestep, offset for clarity. For each of the four curves shown the results for point

and line contacts are superimposed and it can be seen that there are only minor differences in the pressure distributions and that the film thickness distributions obtained are almost identical. The point contact hydrodynamic equation is formulated using four-node linear quadrilateral elements, and for the purposes of this comparison an identical formulation has been used for the line contact example. Comparison of the pressure profiles shows that the peak asperity pressures are the same for the point and line analyses and that where differences are seen the point contact pressure is of the same form as the line contact but offset to a value of up to 10 per cent higher. Since the smooth surface point contact solution pressure exceeds that of the line contact case by 5 per cent, as discussed above, pressure differences of the order shown in Fig. 2 are to be expected. Within the Hertzian area the maximum difference in film thickness between the two rough surface analyses is 0.035 μm and visible differences can only be seen outside the Hertzian area. This is to be expected as the deflected shapes outside the Hertzian area are different for point and line contacts. Figures 3 and 4 present similar comparisons for two further timesteps during the analysis some 1200 timesteps before and 600 timesteps later than that of Fig. 2 respectively. They show essentially the same outcome: minor differences in pressure with an almost identical film thickness distribution using the two models.

Similar results are seen in the individual timesteps shown in Figs 5 to 8. Figures 5 and 6 show comparisons for two further slide–roll ratio values using the same surface profile (A). Figures 7 and 8 have been obtained using the other two roughness profiles (B and C), illustrated in Fig. 1 with the other conditions unchanged. Profile C has a more aggressive effect on

Fig. 2 Transient pressure and film thickness obtained at a timestep with $\xi = 0.25$ for two rough surfaces having profile A: ——— entrainment centre-line of the point contact solution, ·········· corresponding line contact solution. The two rough surfaces in their contacting configuration are shown below, offset for clarity
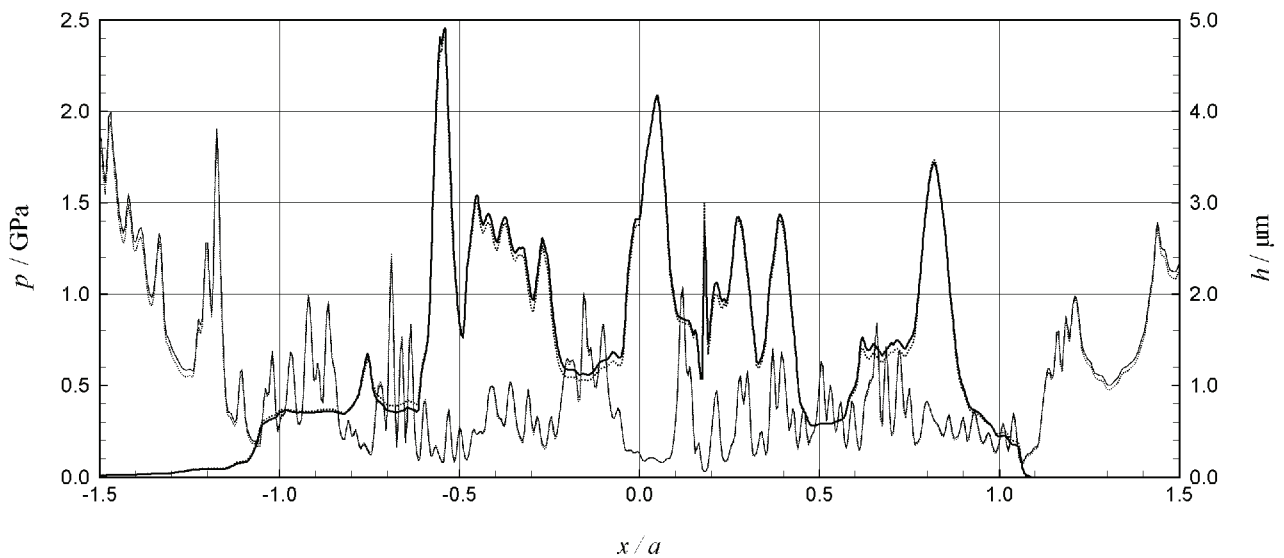
Fig. 3 Transient pressure and film thickness obtained at an earlier timestep with $\xi = 0.25$ for two rough surfaces having profile A: ——— entrainment centre-line of the point contact solution, ·········· corresponding line contact solution

J00303 © IMechE 2003 Proc. Instn Mech. Engrs Vol. 217 Part J: J. Engineering Tribology
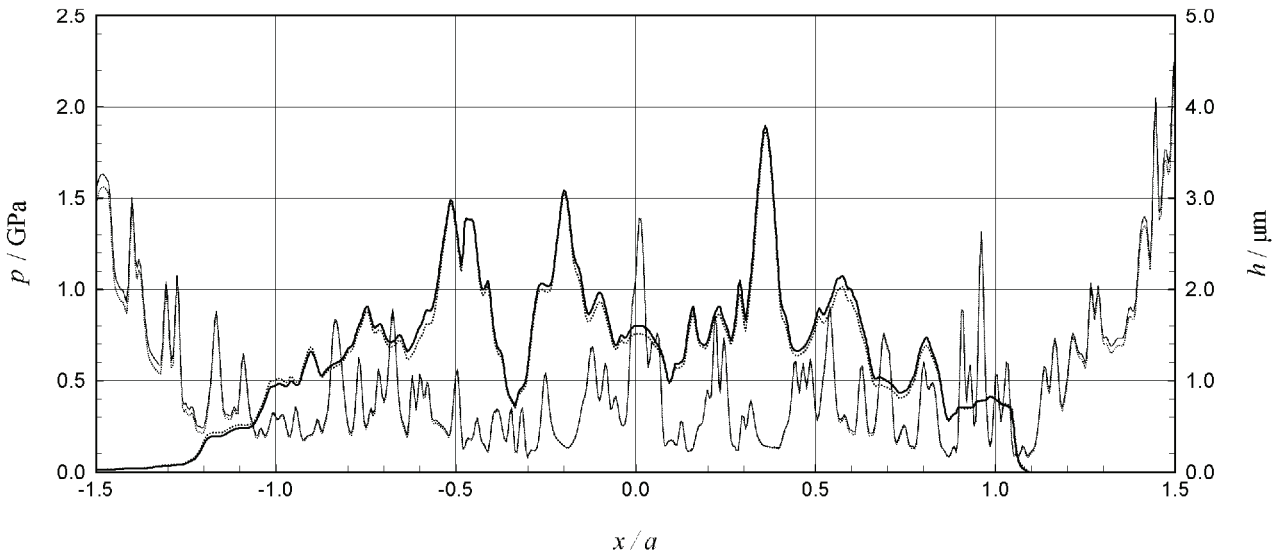
Fig. 4 Transient pressure and film thickness obtained at a later timestep with $\xi = 0.25$ for two rough surfaces having profile A: ———— entrainment centre-line of the point contact solution, $\cdots\cdots\cdots$ corresponding line contact solution

the pressure distribution, as was seen in reference [9], but the salient features of the comparisons between the point and line contact analyses can be seen to be a common feature of all these results.

The comparisons show clearly that in the regime examined where the λ ratio is small, the response of the two surfaces to EHL is essentially the same in the point and line contact cases. This confirms that a line contact analysis is able to predict the rough surface EHL behaviour in the central area of point contacts. The point contact examined in this comparison has an aspect

ratio of about 4:1 so it can be expected that the contacts in involute spur gears, for example, behave in the way predicted by line contact analysis over most of their contact area, given that the ratio of face width to contact dimension is typically greater than 10.

## 3.2 Edge effects in rough point contacts

Although the results reported above clearly indicate the validity of a line contact analysis for the central region
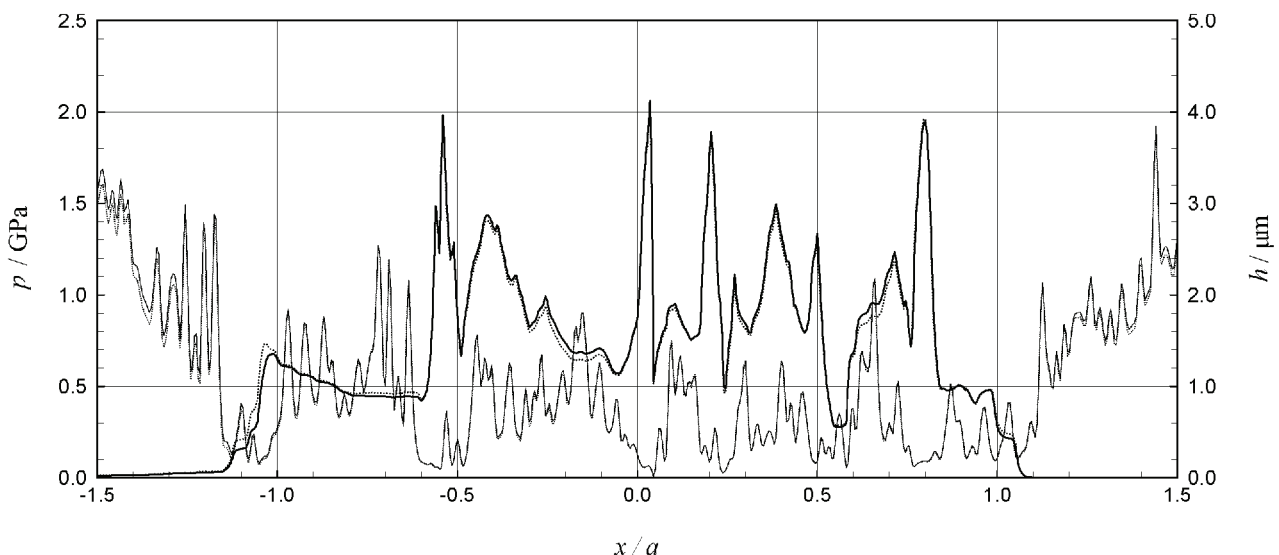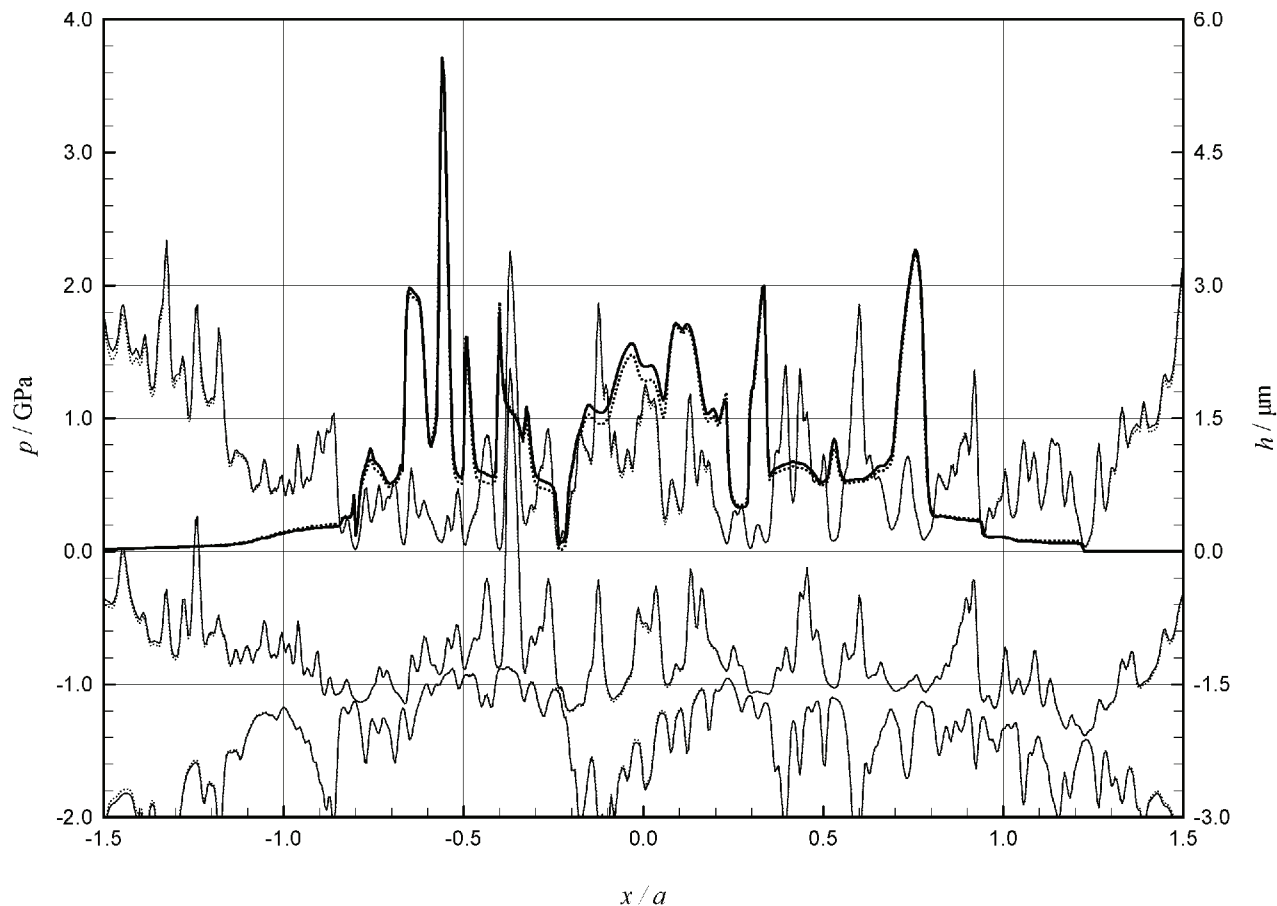

Fig. 5 Transient pressure and film thickness obtained at a timestep with $\xi = 0.1$ for two rough surfaces having profile A: ———— entrainment centre-line of the point contact solution, $\cdots\cdots\cdots$ corresponding line contact solution
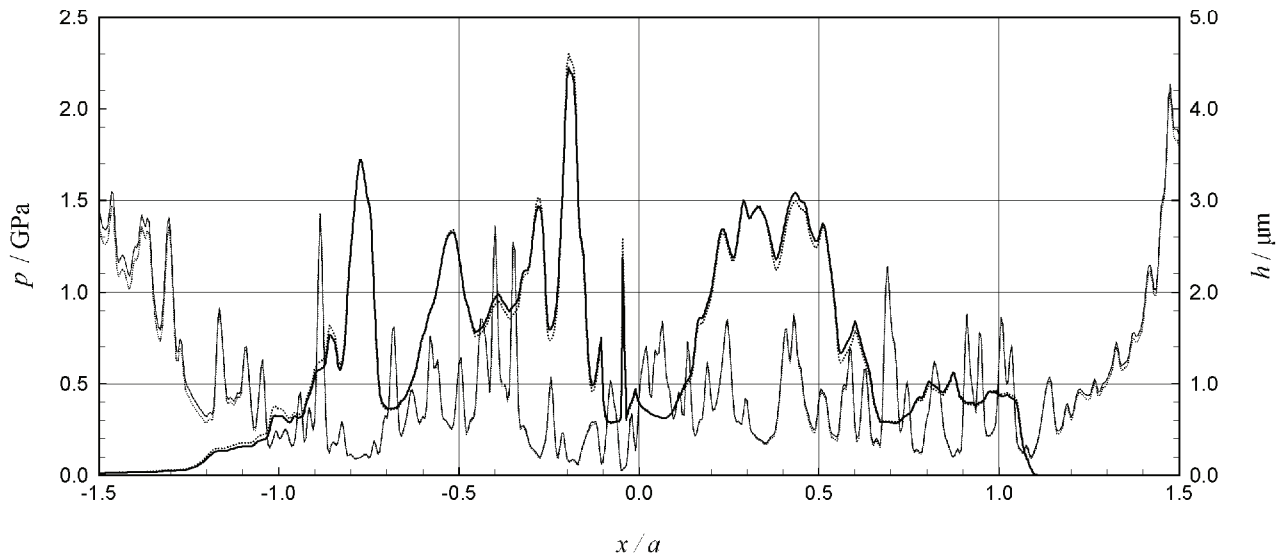
Fig. 6 Transient pressure and film thickness obtained at a timestep with $\xi = 0.5$ for two rough surfaces having profile A: ———— entrainment centre-line of the point contact solution, ·········· corresponding line contact solution
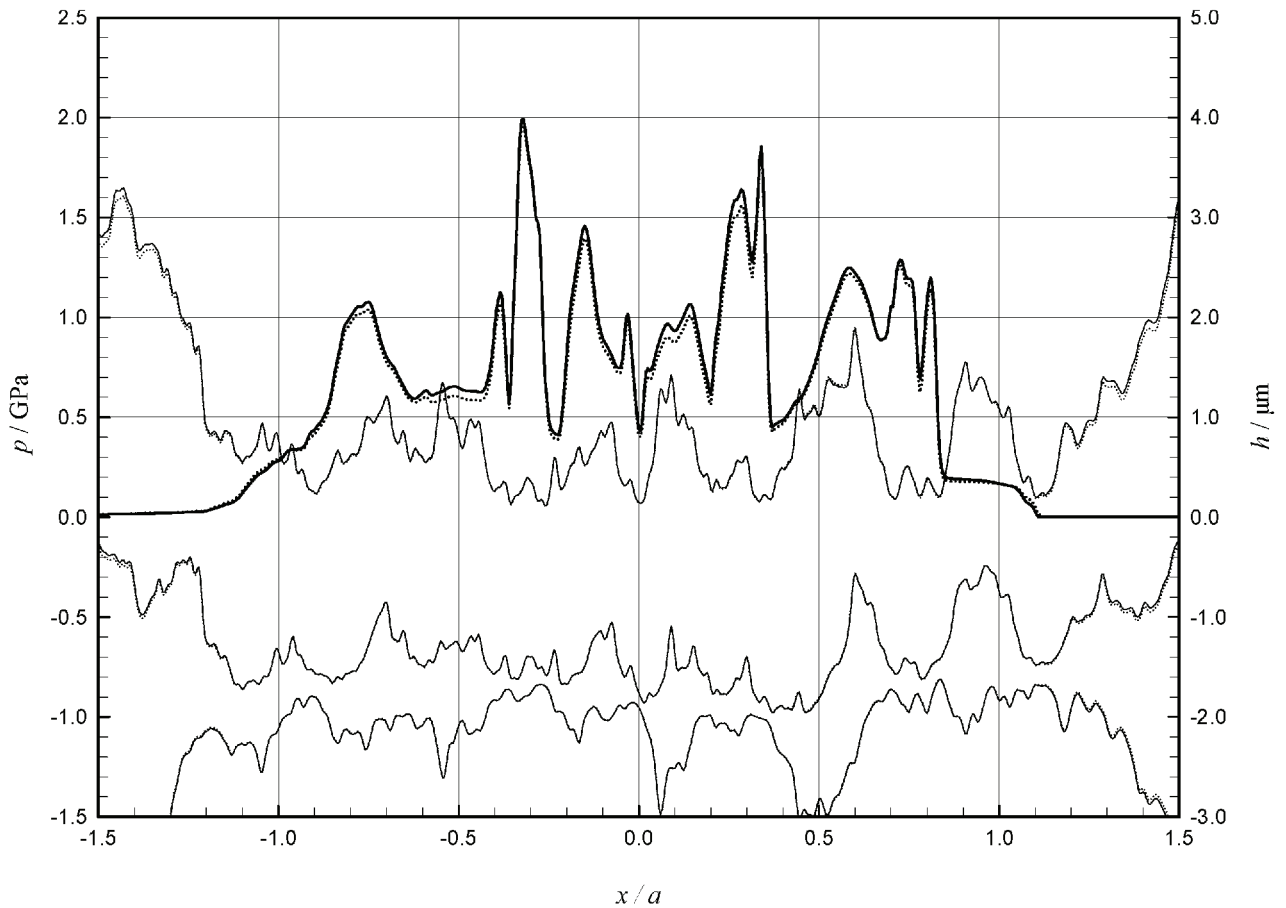
Fig. 7 Transient pressure and film thickness obtained at a timestep with $\xi = 0.25$ for two rough surfaces having profile B: ———— entrainment centre-line of the point contact solution, ·········· corresponding line contact solution. The two rough surfaces in their contacting configuration are shown below, offset for clarity

Fig. 8 Transient pressure and film thickness obtained at a timestep with $\xi = 0.25$ for two rough surfaces having profile C: ——— entrainment centre-line of the point contact solution, ·········· corresponding line contact solution. The two rough surfaces in their contacting configuration are shown below, offset for clarity

of rough surface EHL contacts, there are significant side leakage effects to be observed at the transverse limits of the contact area. Figure 9 shows the film thickness contours obtained for the point contact analysis at the timestep illustrated in Fig. 2. For this example the steady state central film thickness for smooth surfaces is 0.48 μm, with a minimum value of 0.42 μm at the entrainment centre-line. For the timestep shown in Fig. 9, the centre-line film thickness has been reduced by the presence of the moving roughness to have levels of the order of 0.15 μm, i.e. a reduction to 35 per cent of the smooth surface value. The contours show that the film thickness behaviour remains unchanged over most of the width of the Hertzian contact area. Towards the transverse limits of this area, however, the ease with which lubricant in the valley features can move in the transverse direction under the influence of the transverse pressure gradient has a significant influence on the film thickness developed on the microasperities. The authors have previously proposed this as a mechanism for the failure of EHL lubrication with transverse finished surfaces [2], where it was shown that this effect can be

expected to be related to the second derivative of the pressure in the transverse direction, $(\partial^2 p/\partial y^2)$. This is derived from consideration of a rectangular control volume of width δy in the transverse direction that spans a valley feature from one microcontact ridge to the next. The flow out of the control volume in the y direction is given by the integral of $\sigma_y(\partial p/\partial y)$, so the net loss of mass flow is the difference between two such terms on the two sides of the control volume. In simple terms this gives the difference between the flow into the control volume over its upstream boundary of length δy and that out of the control volume at its downstream boundary. The loss of film thickness from one contact ridge to the next is thus due to the integral of $\sigma_y(\partial^2 p/\partial y^2)$ along the valley feature. The location of the highest value of $\partial^2 p/\partial y^2$ in the valley features is included in Fig. 9 as a broken curve. It can be seen that a significant reduction is predicted in the micro film thickness generated between asperities as the edge of the contact is approached and that this reduction is concentrated in the area between the highest value of $\partial^2 p/\partial y^2$ and the transverse edge of the contact.
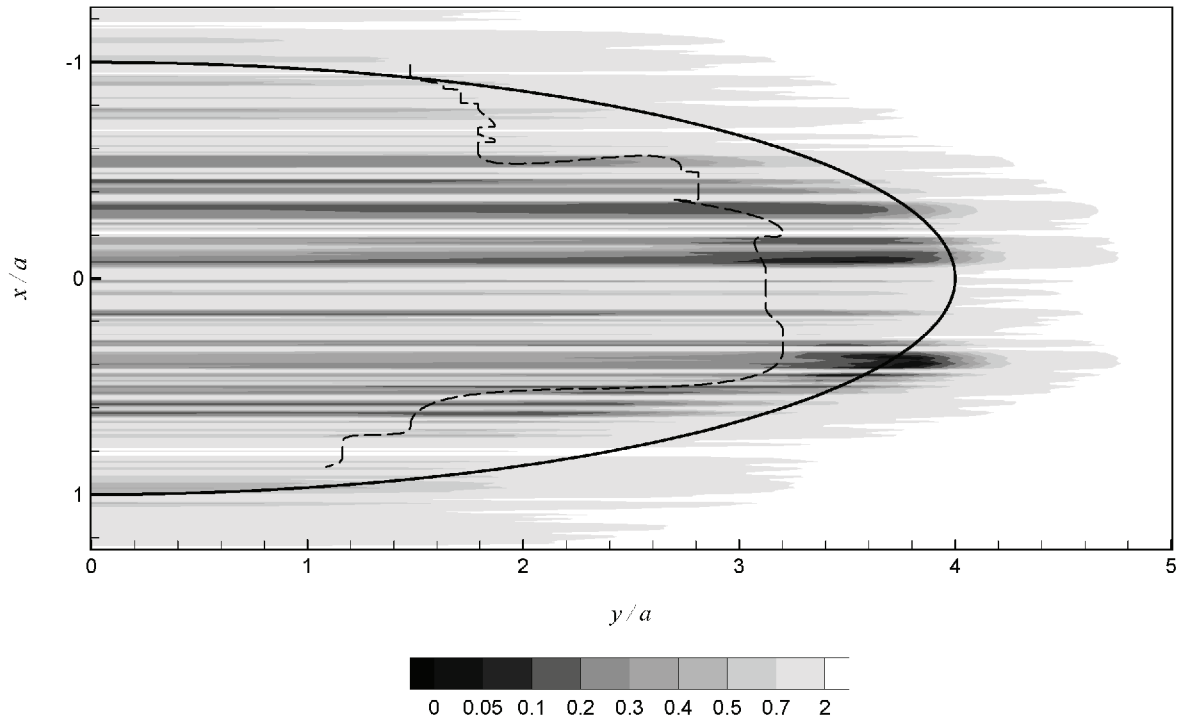
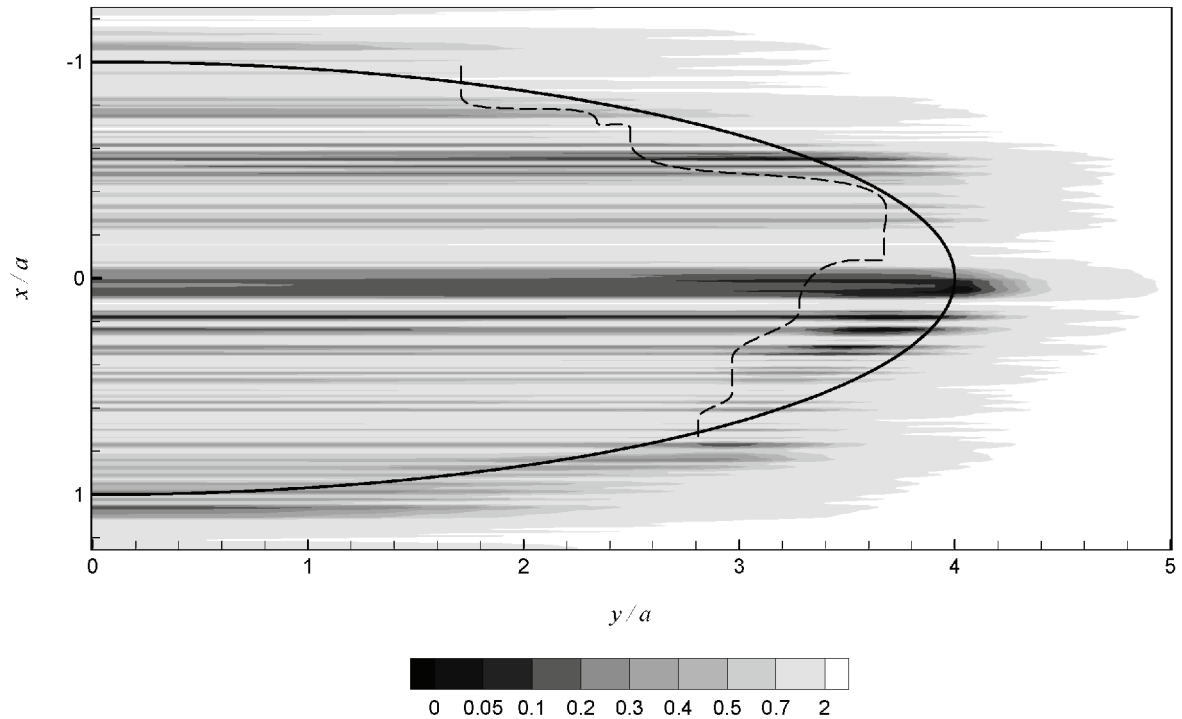**Fig. 9** Film thickness contours (μm) for the point contact solution whose centre-line behaviour is given in Fig. 2. The solid curve indicates the Hertzian contact area and the dashed curve indicates the location of maximum values of $\partial^2 p/\partial y^2$ in valley features

Figures 10 and 11 show film thickness contours for the point contact solutions at the timesteps illustrated in Figs 3 and 4 respectively and confirm the behaviour seen in Fig. 9. The extent of film thinning on an asperity feature can be seen in the transverse sections included in Fig. 12. This shows the transverse film thickness developed in the microcontacts between three pairs of asperities during the analysis. The three asperities are located at $x = -0.187a$, $x = -0.1a$ and $x = 0$ and have centre-line film thickness values of 0.47, 0.34 and 0.12 μm respectively. These values reduce smoothly in the transverse direction, falling by about 7 per cent over the inner half of the contact width. Towards the transverse edge the film thickness values fall sharply to minimum values of 0.22, 0.08 μm and zero respectively in the last 20 per cent of the contact width at that point.

This transverse leakage phenomenon is found to lead to contact conditions developing as the analysis proceeds as described in section 3 and illustrated in the $x = 0$ profile in Fig. 12. To allay concerns as to whether the contact phenomenon described above is unduly influenced by the mesh spacing adopted in the transverse direction, a set of calculations with transverse mesh spacing of $\Delta y = b/50, b/100, b/150$ and $b/200$ was carried out. Figure 13 shows a transverse film thickness section at a timestep in which contact occurs at the location shown. The film profiles for the four transverse mesh resolutions can be seen to follow each other closely. The numbers of contacting mesh points on the

section at the illustrated timestep are 3, 7, 11 and 15 respectively. The corresponding contact lengths are 79, 92, 96 and 98 μm respectively, so that the coarsest resolution contact length agrees with the finest resolution length to within a mesh spacing. In addition, Table 2 gives the number of mesh points in contact at 11 timesteps in the analysis. The last three columns give the numbers for the finer mesh spacings normalized with respect to those for the coarsest. These normalized values are sufficiently close to the ideal values of 2.0, 3.0 and 4.0 to give high confidence that the incidence of contact is being determined to within the resolution of the mesh adopted and that the resolution of $\Delta y = b/50$ adopted in determining the results in this paper is certainly sufficient to identify and quantify the contact phenomenon.

The flow pattern that gives rise to these side leakage effects is illustrated in Fig. 14. This shows a detailed contour plot of film thickness over a limited part of the contact area that contains three microcontacts. The area shown is near the transverse boundary to the Hertzian contact area whose position is indicated by the heavy curve. The composite valley features separating the microcontacts have film thickness values in excess of 1 μm while the microcontact at $x = 0.16a$ has a film thickness that falls as low as 0.05 μm. Vectors of the film's mass flowrate at the timestep illustrated are shown in the figure as arrows aligned with the local flow direction whose lengths are proportional to the flowrate.

Fig. 10 Film thickness contours (μm) for the point contact solution whose centre-line behaviour is given in Fig. 3. The solid curve indicates the Hertzian contact area and the dashed curve indicates the location of maximum values of $\partial^2 p/\partial y^2$ in valley features
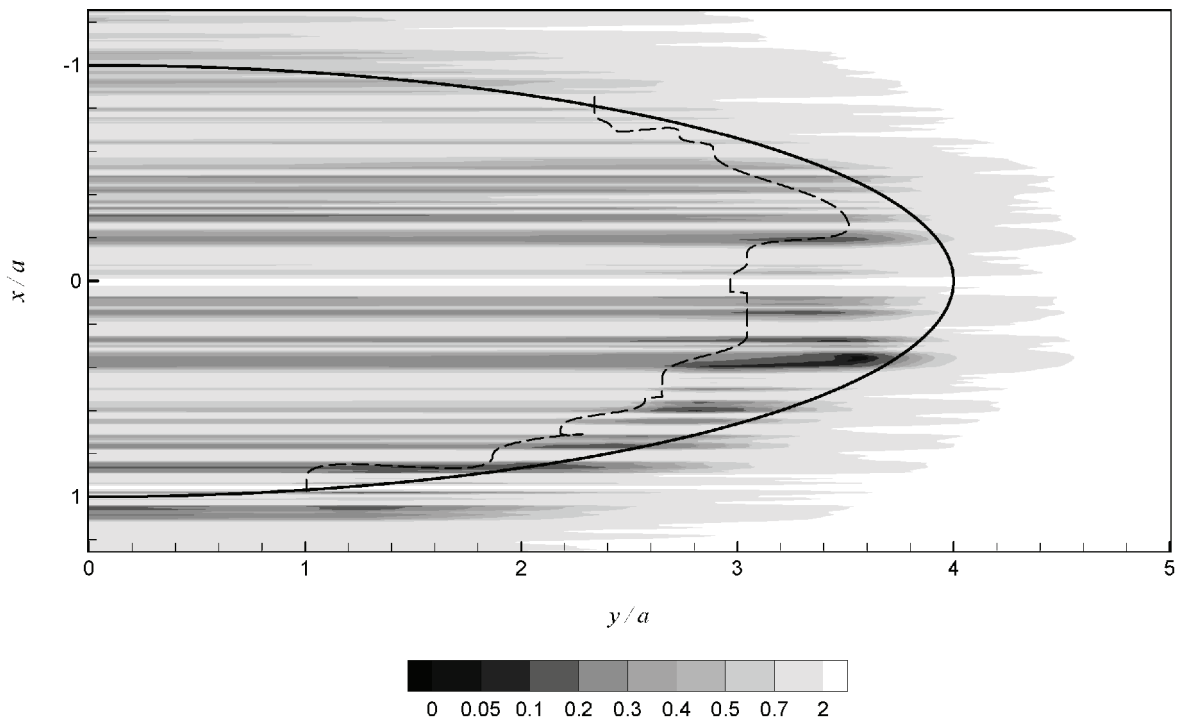
Fig. 11 Film thickness contours (μm) for the point contact solution whose centre-line behaviour is given in Fig. 4. The solid curve indicates the Hertzian contact area and the dashed curve indicates the location of maximum values of $\partial^2 p/\partial y^2$ in valley features
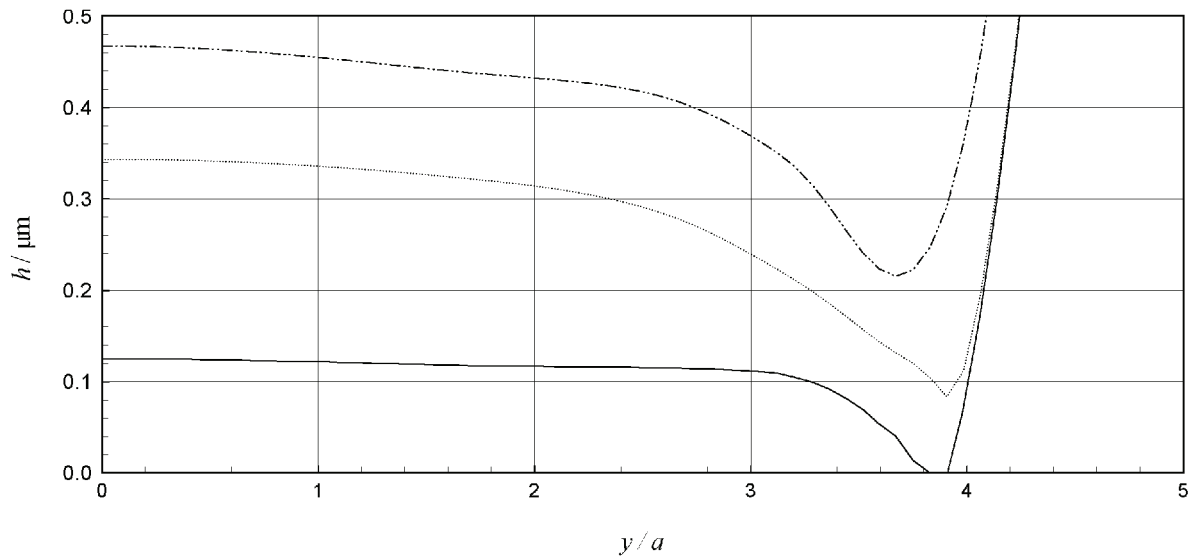

Fig. 12 Transverse film thickness sections for three composite microasperities obtained at a timestep during the point contact analysis of surfaces A with $\xi = 0.25$: ─·──·─ $x = -0.185a$, ········ $x = -0.1a$, ─────── $x = 0$

This illustrates the high degree of deviation of the flow from the rolling/sliding direction that occurs at this transverse boundary, in keeping with the principles of the side leakage mechanism described above.

Figure 15 shows the mesh point locations at which contact of this kind is calculated to occur during 4200 timesteps of the analysis. During this time the slowest moving surface passes through a distance of $9.5a$ relative to the point of contact and the behaviour may be taken as representative of mean behaviour. The count of timesteps during which contact occurs at a mesh point is

indicated by the contour level, so that the darkest colour in the figure corresponds to the highest occurrence of calculated contact. When contact occurs on the entrainment centre-line it also occurs on that particular asperity across the transverse width of the contact. However, this occurrence can be seen to be infrequent from the contours in Fig. 15. The calculated incidence of contact is seen to be concentrated around the transverse boundary of the Hertzian ellipse and to be more prevalent towards the exit of the contact. Both of these features are predicted by the simplified analysis pre-
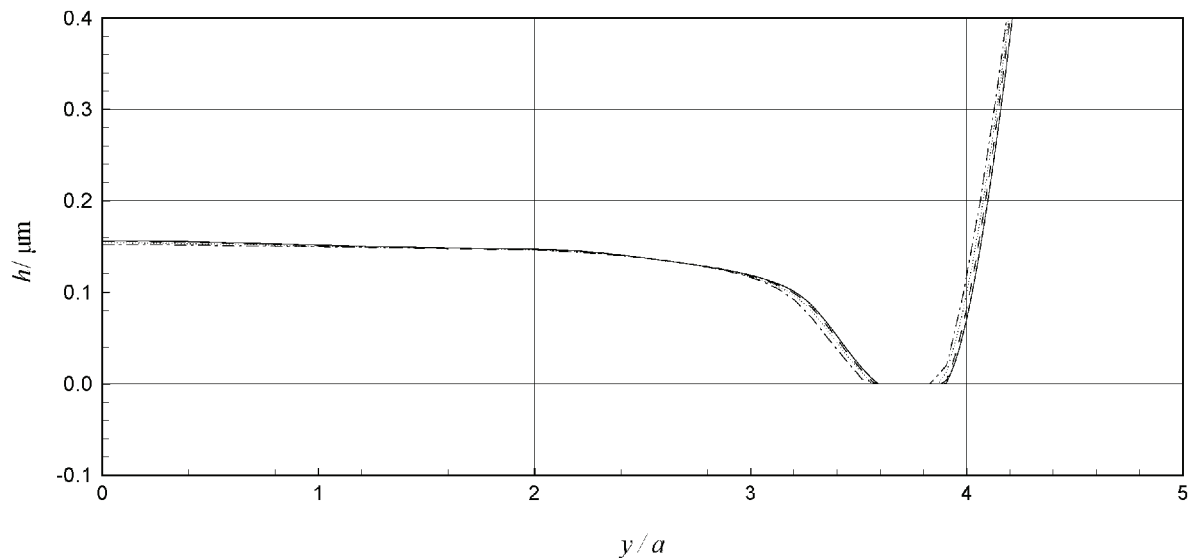
Fig. 13 Transverse film thickness obtained for models with $\Delta x = a/200$ and with different transverse mesh spacing at $x = 0.16a$ for a timestep where contact occurs at that location: ─·──·─ $\Delta y = b/50$, ········ $\Delta y = b/100$, -------- $\Delta y = b/150$ and ─────── $\Delta y = b/200$
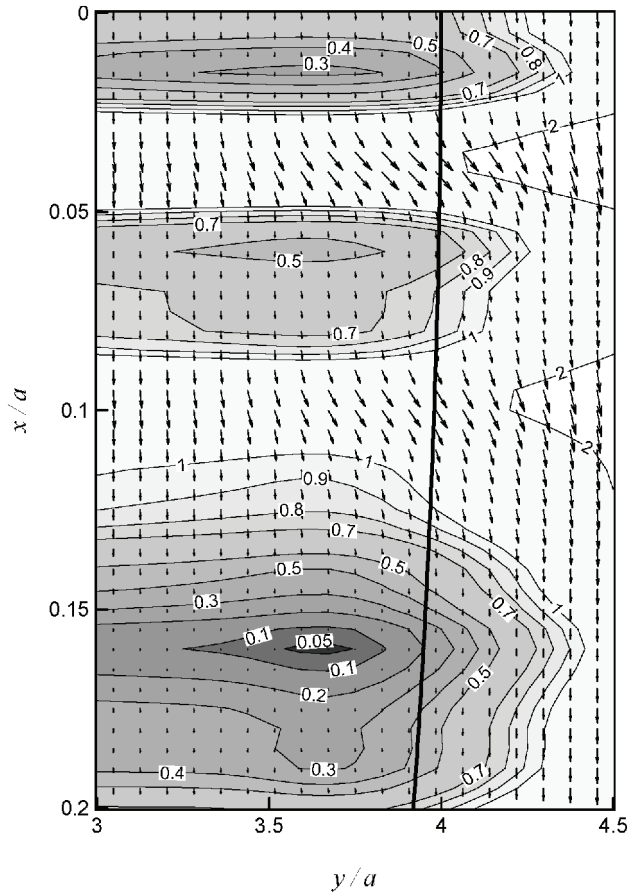
Fig. 14 Detailed contour plot of film thickness over a limited part of the contact area containing three microcontacts with the transverse boundary to the Hertzian contact area included as a heavy curve. Arrows indicate vectors of the lubricant film mass flowrate

progressively weakened at each successive downstream microcontact. This new numerical result for predicted contact also correlates well qualitatively with the observed behaviour of transverse ground discs in scuffing experiments [3]. These discs are found, without exception, to scuff initially at a transverse edge of the contact. The scuffing scar then spreads towards the centre of the contact. Figure 16 shows a photograph of a disc from a typical scuffing experiment of this kind. The transverse grinding marks can be seen both in the central contact track of the crowned disc and in its unloaded parts to the left and right of the contact track. The Hertzian contact area at the scuffing load is illustrated by the overlaid ellipse, and the scuffing damage can be clearly seen to be limited to an area that corresponds to the high contact occurrence locations shown in Fig. 15. In this experiment the load was removed as soon as scuffing was detected by a sharp increase in friction and noise [3], and 75 per cent of the contact area track remains undamaged.

For the elliptical contact results described above the computing mesh covered the area $-2.5a < x < 1.5a$, $-2b < y < 2b$, with mesh spacing $\Delta x = a/200$, $\Delta y = b/50$. The timestep adopted was $\Delta t = \Delta x/(2u_{max})$ so that the faster moving surface moved through one mesh spacing over two timesteps. This aspect of the results has been discussed in some detail in reference [1]. The question of grid point resolution arises and the possible effect of that resolution on calculated contact conditions. The systematic evaluation of this possible feature of the analysis is on-going. However, some confidence that the mesh resolution in the roughness direction is sufficient may be gleaned from Fig. 17. This shows a number of pressure and film thickness sections for the case of Fig. 2 in detail for the area $0.275a < x < 0.475a$. The sections are parallel to the x axis at a number of transverse positions in the Hertzian contact area. The three composite microasperities at $x = 0.3a$, $x = 0.4a$, $x = 0.45a$ can also be observed at a

viously proposed [2], where the film leakage effect was seen to accumulate as the oil moved through the contact with the micro-EHL film-forming mechanism being

Table 2 The number of contacting points at specific timesteps in the analysis carried out with four different transverse mesh spacings. The numbers are also given normalized with respect to those for the coarsest mesh spacing

| Timestep	Number of contacting points in the timestep				Normalized number		
	$\Delta y = b/50$	$\Delta y = b/100$	$\Delta y = b/150$	$\Delta y = b/200$	$\Delta y = b/100$	$\Delta y = b/150$	$\Delta y = b/200$
3550	55	105	155	205	1.91	2.82	3.73
3600	20	35	51	73	1.75	2.55	3.65
3650	35	65	100	131	1.86	2.86	3.74
3700	56	110	162	213	1.96	2.89	3.80
3750	32	61	94	122	1.91	2.94	3.81
3800	122	229	344	457	1.88	2.82	3.75
3850	107	208	309	406	1.94	2.89	3.79
3900	59	113	158	211	1.92	2.68	3.58
3950	88	174	264	352	1.98	3.00	4.00
4000	52	98	146	190	1.88	2.81	3.65
4050	74	140	203	275	1.89	2.74	3.72
Total	700	1338	1986	2635	1.91	2.84	3.76
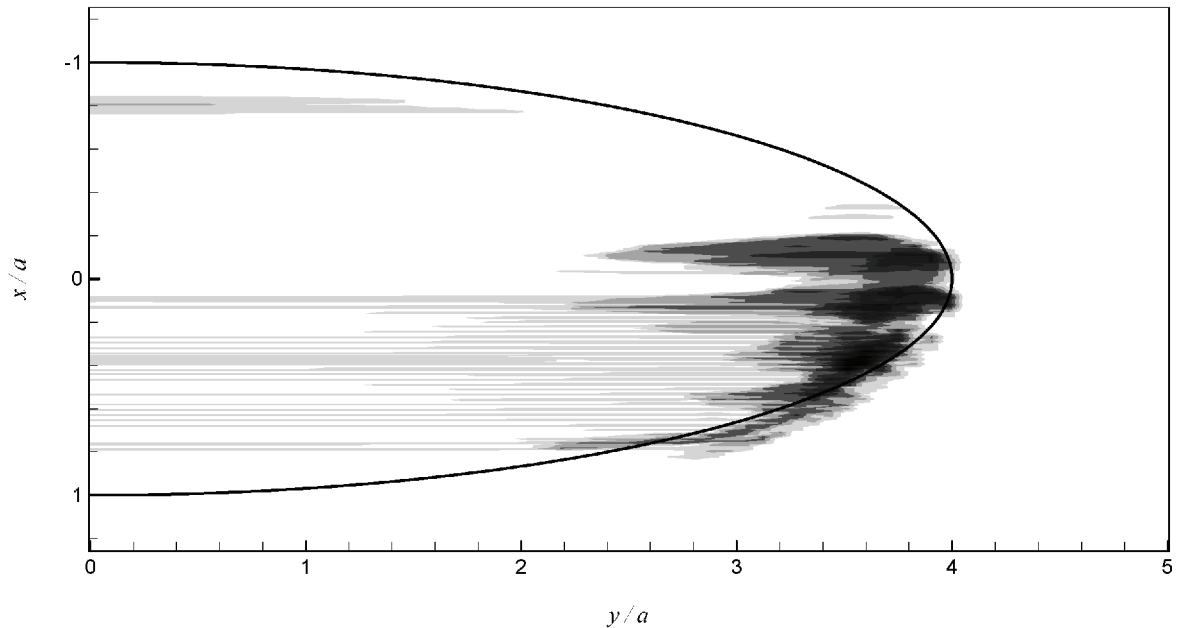
Fig. 15 Illustration of the points at which contact is calculated during 4200 timesteps of the point contact analysis of surfaces A with $\xi = 0.1$. Countours shown indicate the number of timesteps at which a mesh point was calculated to be in contact during the analysis, with darker colours indicating higher values

smaller scale in Fig. 2. The composite microasperity at $x = 0.4a$ is calculated to be in contact at location $y = 3.83a$. Also shown in the figure is the instantaneous composite undeformed roughness, which may be compared with the film thickness sections to examine the asperity deflection taking place in the model solution. The mesh resolution in the direction of this section is the
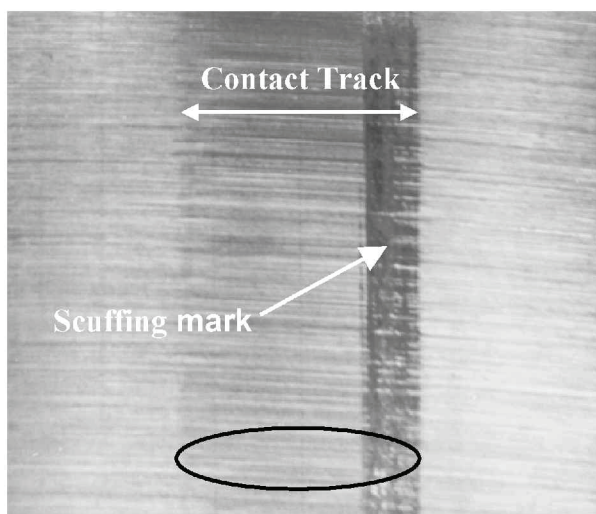
Fig. 16 Photograph of part of the surface of a crowned disc used in the scuffing experiments where scuffing has occurred and the load quickly removed. The location of the elliptical contact area is indicated together with the contact track and scuffing damage mark

same for each of the sections shown, as they differ only in the y location. At the centre-line the microasperity in question develops a film thickness of $0.29\,\mu m$ and generates a pressure of between 1.8 and 2.5 GPa over its deformed width of about $25\,\mu m$ (from $x = 0.34a$ to $x = 0.42a$). When the same section is considered at locations further from the x axis the microasperity film thickness remains at close to the same value over 50 per cent of the Hertzian contact width. This thickness falls (as illustrated in Fig. 12) for sections approaching the transverse edge of the Hertzian contact. At location $y = 3a$ the deflected shape of the composite asperity has changed and developed an exit constriction of $0.04\,\mu m$. Although the pressure generated still reaches 2 GPa, the amount of load carried by the asperity has reduced considerably as the pressure developed in the valley feature centred at $x = 0.325a$ has fallen to below 0.2 GPa. This exit constriction becomes a calculated contact at $y = 3.83a$, and that contact is made without a significant increase in the asperity pressure level, which has in fact fallen to 0.75 GPa at this location. The load carried by the asperity has fallen to 20 per cent of the centre-line value at $y = 3.5a$ and as low as 5 per cent of the centre-line value at $y = 3.8a$. The deflected asperity shape at these sections can be seen to be quite different, indicating that the mesh resolution adopted is not restricting the calculated deflection to an extent that interferes with the numerical model's ability to calculate a full film. The difference between these locations is not in their respective resolution but rather in the degree to which the entrainment mechanism forces lubricant to flow under
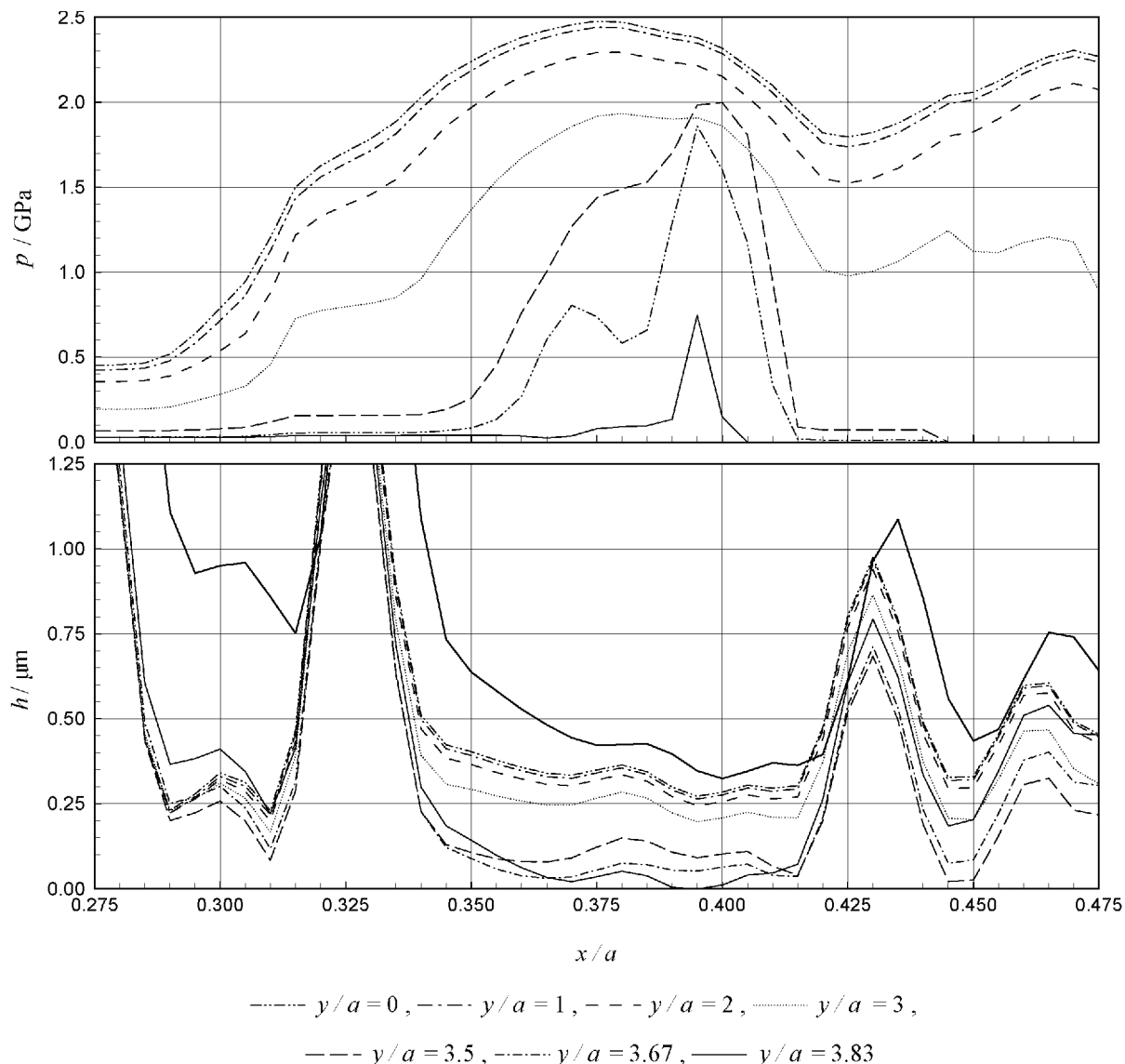
Fig. 17 Comparison of pressure and film thickness variations in the entrainment direction at different transverse locations within the contact for a short section of the composite rough surface. The undeformed composite roughness is also shown as the upper solid curve

the composite asperity separating the contacting surfaces. As the side leakage opportunity increases towards the transverse contact limits, less lubricant is forced under the asperity whose film thickness decreases progressively until the surfaces make calculated contact. It is interesting to note that calculated contact does not necessarily imply elevated pressures.

3.3 Comparison with the results of Zhu [4, 5]

Zhu and colleagues have published the results of a series of investigations showing microcontact between rough surfaces produced by a range of manufacturing processes showing differing degrees of contact between the

surfaces. In recent papers the same method has been applied to surfaces having analytically defined sinusoidal features [**4**] and smooth surfaces subject to extremes of loading [**5**]. The transient analysis described in the current papers has been applied to these conditions for the purposes of comparison, and for this study the mesh sizes and lubricant properties are as specified in references [**4**] and [**5**].

For the smooth surface cases examined in reference [**5**] the results presented by Zhu show a collapse of central film thickness as the load is increased. The particular case chosen for comparison is a circular contact with an entrainment speed of 0.625 m/s. The results shown in reference [**5**] for central film thickness variation with load depart from the Hamrock and Dowson [**10**] line for
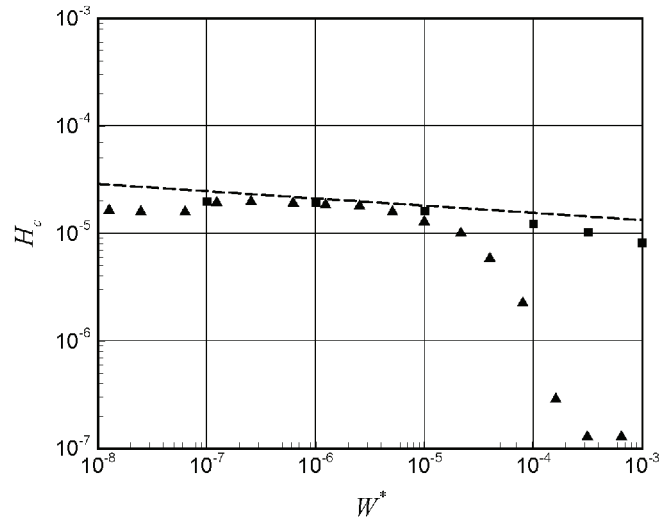
Fig. 18 Variation of dimensionless central film thickness, H_c, with load, W^*, for circular contact with $U = 0.625 \, \text{m/s}$: ▲ results taken from Fig. 5 of reference [5], ■ current results and ------- results from the Hamrock and Dowson formula

$W^* > 5 \times 10^{-6}$, thereafter falling to zero by $W^* > 4 \times 10^{-4}$. In contrast, the current method shows that full films are maintained on the centre-line over the whole extensive range of conditions considered by Zhu. The difference is illustrated in Fig. 18. This shows that the current method calculates central film thickness values that continue to follow the power law behaviour of the Hamrock and Dowson formula at heavier loads while the central film thickness results presented by Zhu fall rapidly to zero.

Comparisons with Zhu and Hu's results for sinusoidal features [4] are made in Fig. 19. The case considered is a circular point contact where both surfaces have features whose heights vary sinusoidally in both the x and y directions. The composite root mean square roughness is $0.4 \, \mu\text{m}$ and the sinusoidal surfaces each have wavelengths of $0.25a$ in the x direction and $1.5a$ in the y direction. The entrainment velocity is again $0.625 \, \text{m/s}$ and the slide–roll ratio is $\xi = -0.2$. This results in a smooth surface solution that has a central film thickness
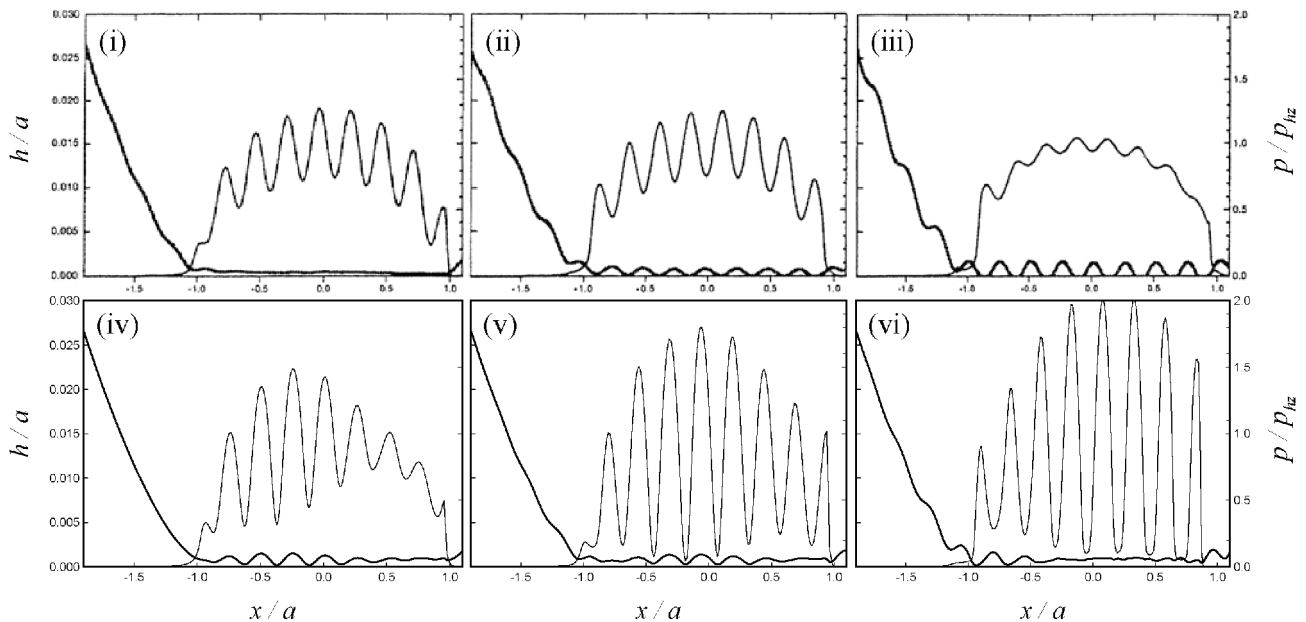
Fig. 19 Variation of pressure and film thickness on the centre-line of circular point contact with both surfaces subjected to sinusoidal waviness in the x and y directions: (i), (ii) and (iii) are taken from reference [4] with waviness asperities, out of phase, offset by $\frac{1}{4}$ wavelength and in phase respectively; (iv), (v) and (vi) are the corresponding results obtained with the current method

of 0.32 μm, a minimum film thickness of 0.12 μm located in transverse lobes and a minimum film thickness of 0.28 μm on the entrainment centre-line. The results presented by Zhu and Hu [4] for this case (Figs 19(i), (ii) and (iii) which are reproduced from reference [4]) predict considerable surface contact on the centre-line as the sinusoidal roughness features move in and out of phase due to the sliding motion. Figure 19(i) represents a timestep where the peaks of one surface are aligned with the troughs of the other, Fig. 19(iii) is a timestep where the peaks of both surfaces are aligned and Fig. 19(ii) is an intermediate situation.

For Fig. 19(i) a full film is shown at each point, with pressure oscillations having an amplitude of about $0.26p_{hz}$ over the Hertzian region. For Fig. 19(ii) contact is shown to occur at seven locations on the centre-line and the pressure oscillations have an amplitude of about $0.23p_h$. For Fig. 19(iii) eight individual microcontacts are shown on the entrainment centre-line and contact occurs over some 40 per cent of the Hertzian contact diameter. The pressure oscillations occurring are much reduced, however, to an amplitude of about $0.06p_h$.

The corresponding results obtained using the current method are shown in Figs 19(iv) to (vi) respectively. These results show no contact occurring on the entrainment centre-line for these cases, which is the case on the centre-line throughout the analysis. For Fig. 19(iv) the calculated minimum film thickness is 0.094 μm at $x/a = -0.35$. For Fig. 19(v) the calculated minimum film thickness is 0.13 μm at $x/a = -0.18$. For Fig. 19(vi) the minimum film thickness shown at $x/a = -0.94$ is 0.084 μm and the film thickness for $x/a > -0.5$ is between 0.2 and 0.5 μm in the Hertzian area. The film thickness results are clearly quite different to those given in reference [4]. The pressures corresponding to the film thickness also differ markedly. The current results show pressure ripples increasing (rather than diminishing) as the surface peaks move into phase and for Fig. 19(vi) the pressure ripple amplitude is $0.95p_{hz}$. The pressure results in reference [4] show markedly less rippling; indeed, in the case of Fig. 19(iii) the pressure presented is quite close to Hertzian. Care was taken to ensure that the mesh size adopted for the current work was the same as that used in reference [4]. Contact is observed with the current method, but very infrequently, and again is located at the transverse limit of the contact area.

In Zhu's theoretical formulation, terms are removed from the Reynolds equation when the film thickness reaches a small but arbitrary value, h_{dry}. The results obtained by Zhu are not sensitive to the particular value adopted for parameter h_{dry} (D. Zhu, personal communication, 2000), but are clearly different to those obtained with the current method, as seen from Fig. 19. The current method has been validated for transient full-film conditions [1] against the independent method

presented by Venner and Lubrecht [11], so there is confidence that its results are correct in full-film cases. The comparison in Fig. 19 shows that the current method predicts a full-film solution, whereas Zhu and Hu's solution shows considerable contact. This difference is disquieting because meaningful study of mixed lubrication must require contact to be established in a consistent way.

The modification of the Reynolds equation introduced by Zhu for positions where the film falls below h_{dry} leads to it becoming

$$\frac{\partial(\rho \bar{U} h)}{\partial x} + \frac{\partial(\rho \bar{V} h)}{\partial y} + \frac{\partial(\rho h)}{\partial t} = 0$$

and it would seem that this simplification, although allowing 'mixed' lubrication calculations, has the effect of causing areas where the film thickness falls below h_{dry} to expand in a way that violates the mass flow continuity that is the foundation of the Reynolds equation. In contrast, the current method maintains all terms in the Reynolds equation, and thus the mass flow balance, for all points where a film is calculated. When contact occurs at a node, h is zero and the Reynolds equation does not apply. The pressures calculated at the contacting points are predicted as a result of applying the differential deflection equation (2) along with the boundary condition $h = 0$ at the contacting points. The pressures developed at the contacting points are then natural boundary conditions for pressure when applying the Reynolds equation at adjacent, non-contacting points. In this way continuity of mass flow is maintained.

4 CONCLUSIONS

1. Results of comparisons between point contact and line contact solutions for low λ EHL situations with transverse roughness show that a line contact analysis is sufficient to determine conditions of pressure and film thickness on the centre-line of the contact. By implication, line contact analyses are able to determine the film behaviour over most of the contacting region in involute gear contacts, for example.

2. Edge effects have been shown to be significant at the transverse margins of contacts between components having a ground surface finish transverse to the entrainment direction. The loss of film thickness in these instances is explained by transverse leakage in the valley features of the composite surface in accordance with the model proposed previously by the authors [2].

3. Direct contact between the surfaces at the transverse boundaries of the conjunction has been observed in calculated EHL solutions, which is consistent with

the location of initial scuffing failure in disc experiments with such surfaces [**3**].
4. The 'mixed' lubrication behaviour predicted by other researchers [**4,5**] who have used a simplified form of the Reynolds equation is not found in the current work when the same conditions are modelled.

ACKNOWLEDGEMENTS

REFERENCES

1 Holmes, M. J. A., Evans, H. P., Hughes, T. G. and **Snidle, R. W.** Transient elastohydrodynamic point contact analysis using a new coupled differential deflection method. Part 1: theory and validation. *Proc. Instn Mech. Engrs, Part J: J. Engineering Tribology*, 2003, **217**(J4), 289–303.

2 Evans, H. P. and **Snidle, R. W.** A model for elastohydrodynamic film failure in contacts between surfaces having transverse finish. *Trans. ASME, J. Tribology*, 1996, **118**, 847–857.

3 Patching, M. J., Kweh, C. C., Evans, H. P. and **Snidle, R. W.** Conditions for scuffing failure of ground and super-finished steel disks at high sliding speeds using a gas turbine engine oil. *Trans. ASME, J. Tribology*, 1995, **117**, 482–489.

4 Zhu, D. and **Hu, Y.-Z.** Effects of rough surface topography and orientation on the EHD and mixed lubrication characteristics. In Proceedings of the International Tribology Conference, Nagasaki, Japan, 2000, pp. 625–630.

5 Zhu, D. Elastohydrodynamic lubrication in extended parameter ranges—Part II: load effect. *Tribology Trans.*, 2002, **45**, 549–555.

6 Elcoate, C. D., Evans, H. P., Hughes, T. G. and **Snidle, R. W.** Transient elastohydrodynamic analysis using a novel coupled differential deflection method. *Proc. Instn Mech. Engrs, Part J: J. Engineering Tribology*, 2001, **215**(J4) 319–337.

7 Holmes, M. J. A., Evans, H. P. and **Snidle, R. W.** Comparison of transient EHL calculations with start-up experiments. In Proceedings of 29th Leeds–Lyon Tribology Symposium, Leeds, 2003 (Elsevier, Oxford).

8 Glovnea, R. P. and **Spikes, H. A.** Elastohydrodynamic film formation at the start-up of the motion. *Proc. Instn Mech. Engrs, Part J: J. Engineering Tribology*, 2001, **215**(J2), 125–138.

9 Tao, J., Hughes, T. G., Evans, H. P. and **Snidle, R. W.** Elastohydrodynamic response of transverse ground gear teeth. In Proceedings of 28th Leeds–Lyon Symposium on *Tribology*, Vienna, 2002, pp. 447–458 (Elsevier, Amsterdam).

10 Hamrock, B. J. and **Dowson, D.** Isothermal elastohydrodynamic lubrication of point contacts, Part 3—fully flooded results. *Trans. ASME, J. Lubric. Technol.*, 1977, **99**, 15–23.

11 Venner, C. H. and **Lubrecht, A. A.** Numerical simulation of transverse ridge in a circular EHL contact under rolling/sliding. *Trans. ASME, J. Tribology*, 1994, **116**, 751–761.